RESEARCH

Revisiting Iran's climate classification: A fresh perspective utilizing the köppen-geiger method

Asiyeh Tayebi[1] · Mohammad Hossein Mokhtari[2] · Kaveh Deilami[3]

Abstract

Empirical climate classification is a process that makes environmental conditions understandable to humans by using climatic elements. Köppen-Geiger (KG) is a popular climate classification method that uses long-term precipitation and temperature data to classify climate into five primary groups. However, long-term continuous meteorological data is heavily exposed to data scarcity, particularly in a national scale. This research study addresses this challenge by leveraging satellite imageries, multilinear regression models and spatial interpolation within the context of entire country of Iran between 2016 and 2019. Accordingly, this study examined statistical relationship between 14 explanatory variables under four main categories of MODIS-LST, MODIS-NDVI, MODIS-TVDI, GPM-precipitation and SRTM-DEM against ground-based precipitation and temperature data (dependent variables). The spatial interpolation model (i.e. Krigging and Co-krigging) was directly developed from weather observation station datasets. A total of 332 synoptic stations were selected, 67% of which were used in modeling and the remaining 33% in testing. Accuracy assessment was performed with Kappa statistics. Overall, this research study developed three KG classification maps. These include a map per precipitation and temperature from regression model and spatial interpolation and a point-based maps from unused climate data in modelling. This study identified three KG main climate groups of arid, warm temperate and snow and eight KG sub-groups of hot desert, cold steppe, cold desert, hot steppe, warm temperate climate with dry hot summer, snow climate with dry hot summer, warm temperate climate with dry warm summer and snow climate with dry warm summer. A comparison between those maps (kappa = 0.75) showed the higher accuracy of regression-based KG maps against spatial interpolation maps. This study contributes to a more detailed monitor of climate change across countries and regions with sparse distribution of weather observation data.

1 Introduction

Climate classification refers to the grouping of similar conditions through formulating a set of environmental factors. The process generates areas with distinct climatic patterns and provides the possibility of finding localities with similar climate conditions in different geographical areas. Climate classification provides several benefits to agricultural planning, urban planning, risk assessment by insurance companies and governance and obviously climate studies (Fallmann and Emeis 2020). Various models are adopted in climate classification, examples include aridity index, Alisov, Köppen, Berg, Holdridge life zones, Lauer, Strahler, Thornthwaite, Trewartha, Troll, and Vahl. Amongst, Köppen model is widely used across scientific and industry community. The method is a vegetation-based climate classification, which provides a basis to identify climate similarity and dissimilarity (Köppen 1936). This method initially relied on the botanical zones under the influence of climatic conditions, but it was then improved by taking into account meteorological data and presenting climate types through arbitrary indices. Köppen-Geiger (KG) (Geiger 1961) is the final version of Köppen model and the most commonly used method of climate zonation in any geographical location (Sohoulande 2024). All that it requires is temperature and precipitation

✉ Mohammad Hossein Mokhtari
  mh.mokhtari@yazd.ac.ir

  Asiyeh Tayebi
  asiyeh.tayebi@gmail.com

  Kaveh Deilami
  Kaveh.deilami@rmit.edu.au

1 Department of Geography, Yazd University, Yazd, Iran

2 Department of Arid Land and Desert Management, Faculty of Natural Resources, Yazd University, Yazd, Iran

3 Centre for Urban Research, RMIT University, Melbourne, VIC 3000, Australia

ground datasets (Ascencio-Vásquez et al. 2019; Hobbi et al. 2022).

The potential of the KG model to quantify climate variation and change over various periods has been demonstrated in previous studies (Cui et al. 2021). Due to its relevance to ecological conditions, this method can serve to classify the various aspects of the environment objectively from practical and theoretical points of view, such as photovoltaic climate zonation (Ascencio-Vásquez et al. 2019; Mazzeo et al. 2020), development of diffuse irradiation models (Every et al. 2020), estimation evapotranspiration in relation to Köppen's method (Akhavan et al. 2018), evaluation of outdoor thermal perception and comfort conditions (Canan et al. 2020; Salata et al. 2018), mapping of the last glacial maximum, mid-holocene, and present climate zones (Yoo and Rohli 2016), and identification of particulate matter clusters (Pražnikar 2017).

The best outcome of KG method relies on long-term and fine resolution ground-based climatic variables (i.e. air temperature and percipitation) (Ouatiki et al. 2023). The data is required for accurate climate zonation, good definition of transition areas, and detection of past and future changes in climate zones (Bonsoms and Ninyerola 2024). However, owing to high costs and accessibility constraints, weather stations are characterized with spatially poor coverage and nonhomogeneous data (Javanshiri et al. 2021). As a result, application of KG method on a massive scale (e.g. national scale) is challanged by data inconsistency and scarcity (Beck et al. 2018; Zou et al. 2021).

To fill the gaps across the ground-based (i.e. data inconsistency and scarcity), two techniques have gained significant attention: (1) integrating satellite-derived climate variables into supervised machine learning (e.g. multilinear regression analysis). This is a statistical model to fill the gaps across ground-based data by developing a best-fit line between alternative sources of data (e.g. satellite images) and available data from weather stations (Aksu et al. 2023; de Moraes and Gonçalves 2023); and (2) Geo-statistical interpolation methods utilize the spatial relationship/equation of the measured sample points to create a continuous map with point data (Atkinson and Lloyd 2014; Madenci et al. 2019). Generally, the principle of spatial prediction means that items that are closer to each other tend to be more similar and vice versa. Obviously, the use of these techniques to generate data for KG method requires considering a diverse range of parameters such as spatial and temporal resolution of data, selection of explanatory variables (herein temperature, elevation and precipitation), data quality of satellite images, and geographical distribution of weather stations (Mokhtari et al. 2013). As a result, robust comparison between these techniques rarely conducted and widely have been limited to small and medium-sized areas (Aboutalebi et al. 2018).

Although satellite data provides continuous information on the spatial data characteristics of features, comparisons indicated a noticeable deviation between satellite precipitation and ground-based measurements in daily, monthly and annual timescales and different spatial scales (Ma et al. 2021). In order to achieve good spatial variation in precipitation and better accuracy than the original image data the least squares linear relationship between remote sensing precipitation data and ground-observed precipitation has been suggested (yosefi kebriya et al. 2021). Therefore, in this study, first, the relationship between ground data and data from satellite sources was examined through MLR method. As a routine procedure, statistical methods based on interpolation techniques are applied for spatial gap-filling of weather data (Hammann and MacDonell 2022). Therefore, the method based on spatial interpolation of point data will be evaluated as an alternative in this study.

Accordingly, within the context of the entire country of Iran, the objectives of this study are threefold: (1) use satellite-derived climate variables within the framework of machine learning, particularly multilinear regression analysis (MLR) to generate air temperature and precipitation for KG method; (2) use spatial interpolation to fill the ground-based climate data for KG classification and (3) Compare KG maps from two previous methods to enhance detection of the climate class boundary and facilitate climate change monitoring.

This study is expected to overcome the shortcoming of generation climate classification maps within the context of an entire country due to unavailability or spatially spars distribution of weather stations. In addition, climate change is expected to be better monitored due to the availability of satellite data on various spatial scales and the advancement of remote sensing technology in the near future.

2 Materials and methods

2.1 Description of the study area

The study area covers the entire country of Iran located in the south-western Asia. It expanses from 25° to 40° North latitude and from 44° to 64° East longitude (Fig. 1). The altitude changes from about -25 m to about 5610 m above sea level significantly contributes to the climatic heterogeneity of this country. (Ghajarnia et al. 2022; Javanshiri et al. 2021; Razmi et al. 2017). Iran is mostly located in arid and semi-arid zones (Fallah et al. 2017). The annual rainfall varies from less than 50 mm in the uninhabitable eastern deserts to 1800 mm on the shores of the Caspian Sea and the Western highlands.

The temperature variation has increased over the last decades, and the mean annual temperature is predicted to
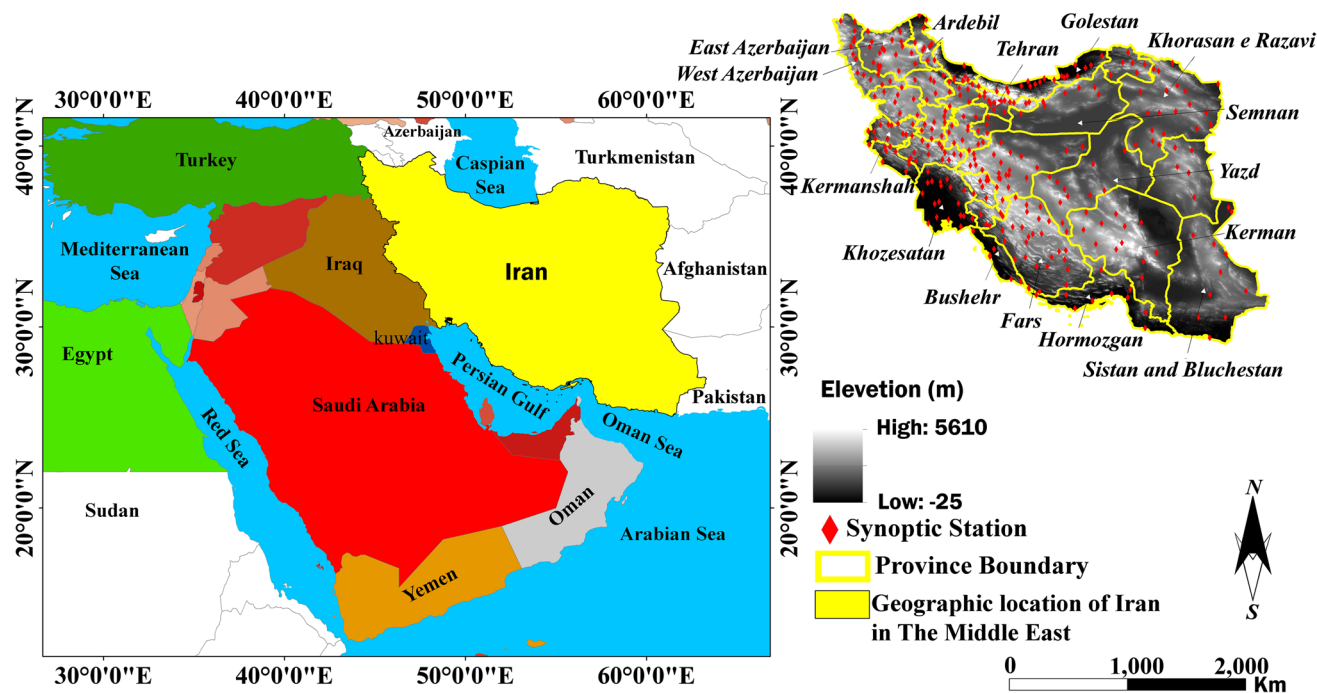
Fig. 1 Map of the study area and the locations of the synoptic weather stations

increase in the next decades from 1.5 to 4.5 degrees centigrade under the scenarios proposed by the Intergovernmental Panel on Climate Change (IPCC). Overall, Iran experiences hyper-arid, arid, semi-arid, Mediterranean, and wet climate (cold mountainous type) with the spatial coverage of 35.5%, 29.2%, 20.1%, 5% and 10%, respectively (Amiri and Eslamian 2010).

2.2 Data

2.2.1 Satellie Dataset

As shown in Table 1, the satellite dataset for this study consists of MODIS/Terra products, GPM IMERG V06 precipitation and Shuttle Radar Topography Mission (SRTM) datasets. The MODIS imageries include LST (MOD11A2) and NDVI (MOD13A3) images with 1000 m spatial resolution for a period from 1 April 2016 to 29

May 15, 2019 on a monthly basis. In total 171 MODIS images were downloaded for this study.

KG method requires monthly base data for climate classification. Therefore, daily, 8-days average data sources were aggregated to be used in KG method. On the other hand, for the climate studies, usually, the data indicating weather patterns at least over the above 30 years are required (Francisco 2014). Since this study evaluates the capability of the aimed methodology, in order to reduce the computational process, the above-mentioned data periods were selected. On the other hand, comparisons of three climate classification approaches based on KG method using the same short-term data, it is expected not to affect the research methodology. Therefore, in case of a virtuous accuracy of the result, the presented methodology can be applied for the data of long-term data to produce a real climate classification map over the study area or anywhere else.

Table 1 Specification of the satellite imageries used in this research study

Date	Image data	Temporal scale	Product type	Spatial resolution (m)	Total images downloaded
1.4.2016 – 29.3.2019	MOD11A2	8 Days average	LST	1000	135
1.4.2016 – 1.3.2019	MOD13A3	Monthly	NDVI	1000	36
1.4.2016 – 29.3.2019	GPM IMERG V06	Daily	Precipitation	10,000	1095
29.11, 2014	SRTM	---	DEM	1000	1

The GPM dataset was obtained from the above period with the spatial resolution of 10,000 m. GPM has approximately ten constellation satellites and a core satellite that was launched on February 27, 2014, with the multi-channel GPM Microwave Imager (GMI). GMI uses a set of frequencies and the first Ku/Ka-band dual-frequency space-based precipitation radar as a reference standard to unify precipitation measurements from a constellation of operational satellites (Ma et al. 2021). Finally, SRTM data with the spatial resolution of 1000m, created on November 29, 2014, was obtained from the USGS official website.

2.2.2 Meteorological data from weather stations

Precipitation and temperature are critical inputs for KG method. Both data are recorded in weather stations and are more available than the other types of climate data anywhere on the earth. In this study, the ground-based temperature and precipitation data were derived from 332 synoptic weather stations located in the 32 provinces of Iran. Subsequently, the ground-based data were aggregated to produce seven meteorological variables including mean temperature of the coldest (T_{min}) and hottest (T_{max}) month, mean annual near-surface temperature (T_{ann}), accumulated annual precipitation (P_{ann}), precipitation of the driest month (P_{min}), lowest and highest monthly precipitation values of summer (P_{smin}) and winter (P_{smax}). The temperature and precipitation data was recorded in Celsius degrees (ºC) and millimeters (mm), respectively.

It should be noted that through stratified sampling, the weather station dataset was split into a modeling dataset and a testing dataset (30%-40%), which is a common practice in research (Deyasi et al. 2021; McGibbon et al. 2023). Accordingly, 33% of weather station data (109 stations) was selected for the evaluation of maps and remaining dataset (223 stations) was used for MLR and spatial interpolation purposes.

2.3 Methods

As shown in Fig. 2, research methodology comprised four main courses (1) modelling air temperature and precipitation values using MLR models from MODIS and GPM satellite imageries; (2) generate air temperature and precipitation values through spatial interpolation (i.e. Krigging and Co-Krigging); (3) produce six KG classification maps. This includes a KG classification map per percipitation and air temperature from MLR model, spatial interpolation and unused meteorological data in MLR model and spatial interpolation technique; and (4) comparing the KG classification maps to determine the most effective and accurate technique.

2.3.1 Developing MLR models using MODIS and GPM data

The first course of methodology focused on developing multiple MLR models between air temperature and precipitation from 223 weather stations (dependent variables) and explanatory variables from MODIS, GPM, and SRTM imageries. It is reported that the linear relationship between remote sensing precipitation products and gauge-measured precipitation could be used to correct and predict satellite precipitation data (Ma et al. 2021). Generally, the linear regression model is presented as follows:

$$Y_i = \beta_0 + \sum_{j=1}^{n} \beta_i x_j + \varepsilon_i \tag{1}$$

where Y_i is i^{th} of dependent variable, β_0 is line interception coefficient, β_i is regression coefficients of ith independent variable, that are determined by fitting the equation to the data, X_i through X_n are the independent variable and ε presents the difference between observed and predicted value of dependent variable. The total variability of dependent variable accounted for by multiple linear regression is measured through coefficient of determination (Tabachnick and Fidell 2007):

$$R^2 = \frac{ss_{reg}}{ss_y} \tag{2}$$

$$ss_y = \sum (y_i - \bar{y})^2, ss_{reg} = \sum (y_i' - \bar{y})^2 \tag{3}$$

where ss_y is the total sum of squares difference between each observed value y and the mean of y over all cases and ss_{reg} is the total sum of squared due to regression calculated from predicted value (y') and the mean of y over all cases. The squared multiple correlation can also be calculated from the sum of the correlation between dependent and independent variable, r_{yi}, and standardized regression coefficient, β_i of independent variable as follow:

$$R^2 = \sum_{i=1}^{k} r_{yi} \beta_i \tag{4}$$

where r_{yi} is the correlation between dependent variable and i^{th} independent variable and β is the standardized regression coefficient that is used to estimate standardized y.

The satellite-based explanatory variables include 20 variables (see Table 2) which can categorized under 4 land surface temperature (LST), normalized difference vegetation index (NDVI), digital elevation model (DEM) and temperature-vegetation dryness index (TVDI). Previous studies have documented these explanatory variables to be the most effective for conducting regression analysis between air temperature and precipitation using data from weather stations and satellites (Hooker et al. 2018; Ouma et al. 2021).
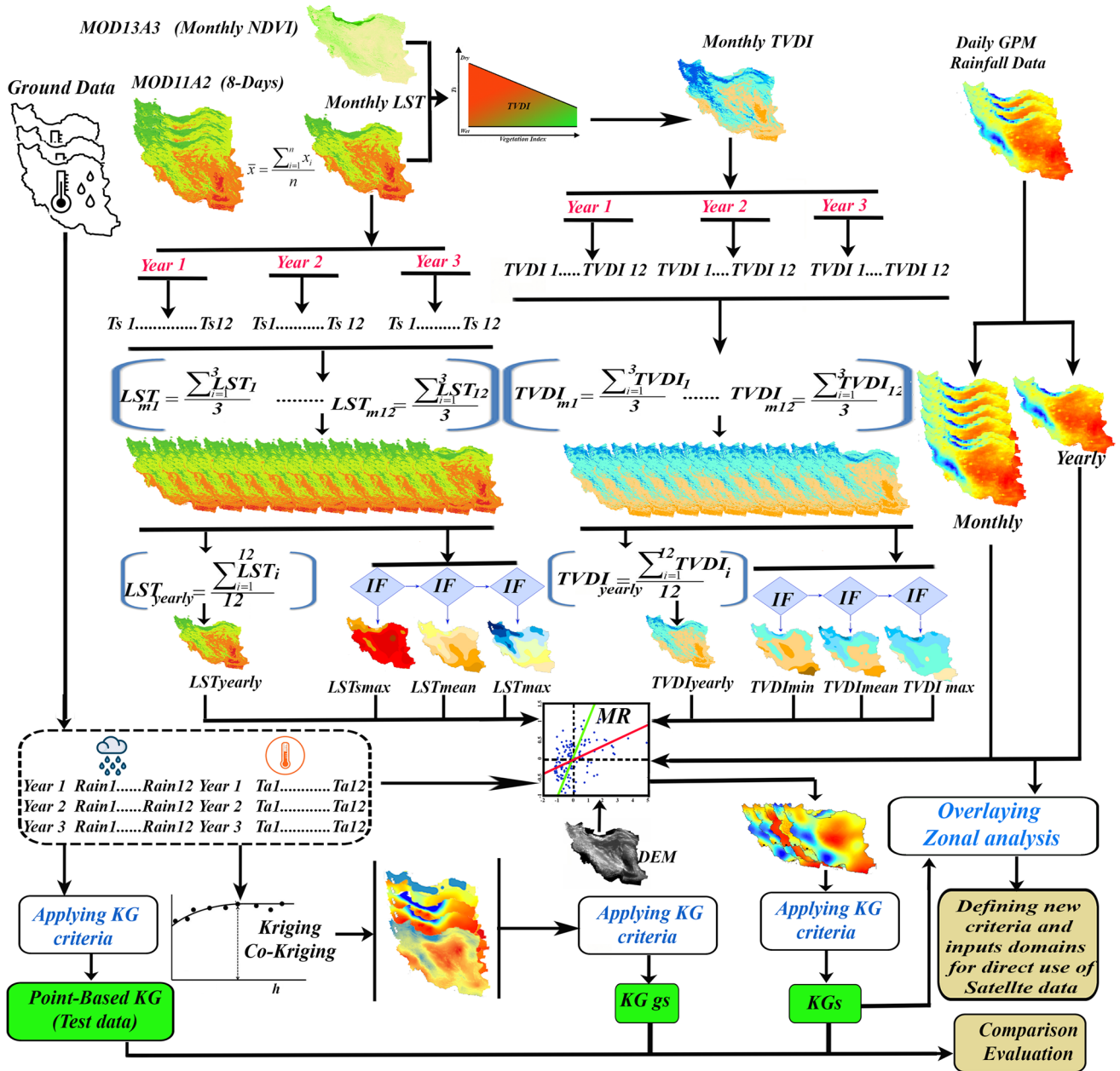
Fig. 2 Research procedure to produce KG classification maps within the context of the entire country of Iran

In order to generate the above data (explanatory variables), initially, the satellite images underwent required reprocessing and processing (i.e. data rescaling and normalization) schemes and finally resampled to 1000 m spatial resolution to be used for further analysis. Subsequently, three types of LST products were generated from MOD11A2 satellite images. These imageries were delivered in an 8-day average; thus, all the image within a month were averaged to produce monthly LST images. This study also produced yearly LST data as follows:

$$\overline{MLST}_i = \frac{\sum_{j=1}^{3} \overline{LST}_{ij}}{3} \tag{5}$$

where $\overline{MLST}_i$ is the mean monthly LST image of the ith month of three years, and $\overline{LST}_i$ is the mean LST image calculated from the three 8-day images acquired in the ith month of the jth year. This study used the data of three years; therefore, the term $\sum_{j=1}^{3} \overline{LST}_{ij}$ was divided by 3.

Table 2 List of satellite-based explanatory variables used in MLR models

| Abbreviation (Explanatory variables)	Definition
GPM_{ann}	Accumulated Annual GPM Precipitation
GPM_{smin}	Lowest Monthly GPM Precipitation Values For The Summer
GPM_w	Mean Value of Winter GPM Precipitation
GPM_{wmax}	Highest Monthly GPM Precipitation Values For The Winter
GPM_{wmin}	Lowest Monthly GPM Precipitation Values For The Winter
LST_{ann}	Annual Mean Land Surface Temperature
LST_{max}	Monthly Mean Land Surface Temperature of The Hottest Month
LST_{min}	Monthly Mean Land Surface Temperature of The Coldest Month
$NVDI_{ann}$	Annual Mean Normalized Difference Vegetation Index
$NDVI_{max}$	Monthly Mean Normalized Difference Vegetation Index of The Hottest Month
$NDVI_{min}$	Monthly Mean Normalized Difference Vegetation Index of The Coldest Month
$NVDI_{smin}$	Lowest Monthly Normalized Difference Vegetation Index Values For The Summer
$NVDI_{wmax}$	Highest Monthly Normalized Difference Vegetation Index Values For The Winter
$NVDI_{wmin}$	Lowest Monthly Normalized Difference Vegetation Index Values For The Winter
$NVDI_{wmin}$	Lowest Monthly Normalized Difference Vegetation Index Values For The Winter
$TVDI_{ann}$	Annual Mean Temperature-Vegetation Dryness Index
$TVDI_{smin}$	Lowest Monthly Temperature-Vegetation Dryness Index Values For The Summer
$TVDI_{wmax}$	Highest Monthly Temperature-Vegetation Dryness Index Values For The Winter
$TVDI_{wmin}$	Lowest Monthly Temperature-Vegetation Dryness Index Values For The Winter
$TVDI_{wmin}$	Lowest Monthly Temperature-Vegetation Dryness Index Values For The Winter
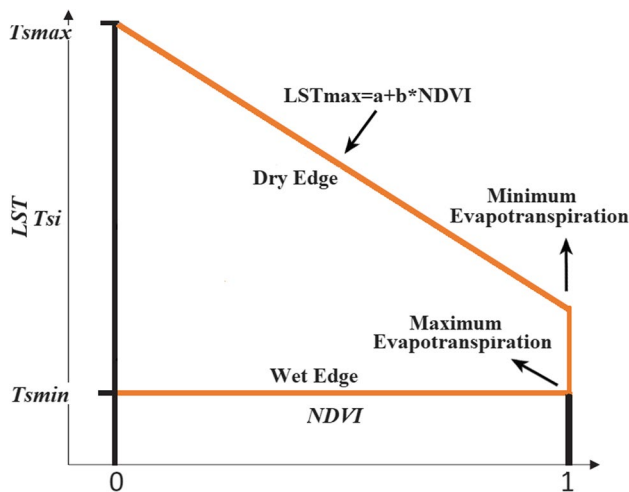
Fig. 3 LST-NDVI triangle space adapted from Sandholt, et al. (2002)

TVDI is a widely used method to derive the spatial variation of soil moisture based on the relationship between LST and normalized difference vegetation index (Fig. 3) calculated from satellite data (Moosavi et al. 2016; Sandholt et al. 2002; Wigmore et al. 2019). TVDI values were calculated from following equations:

$$TVDI = \frac{LST - LST_{min}}{LST_{max} - LST_{min}} \tag{6}$$

where LST is the observed surface temperature, LST_{min} is the wet edge, and LST_{max} is the dry edge that is calculated from Eq. 10.

$$LST_{max} = a + b * NDVI \tag{7}$$

where a and b coefficients are obtained from the linear relationship between LST and vegetation cover, and NDVI is an image calculated from red (R) and near infrared (NIR) satellite data as follows:

$$NDVI = \frac{NIR - R}{NIR + R} \tag{8}$$

TVDI was calculated from the MODIS LST product image (MOD11A2) and the NDVI image (MOD13A3). Like Eq. 2, the monthly NDVI image was calculated from Eq. 6:

$$\overline{MNDVI}_i = \frac{\sum_{j=1}^{3} NDVI_{ij}}{3} \tag{9}$$

where $\overline{MNDVI}_i$ is the mean monthly NDVI image of the ith month of three years, and $NDVI_i$ is the NDVI image of the ith month of the jth year.

In the case of GPM data, the completed half-hourly calibrated IMERG data provided by "precipitationCal " with the "netCDF" file format were converted to the Tagged Image File Format (TIFF). These imageries then used to extract precipitation values for the entire country. Finally, As shown in Table 5 a total of three regression models

were generated between T_{min}, T_{max} and T_{ann} (dependent variables); and $LST_{max}, LST_{min}, LST_{ann}$.

2.3.2 Spatial interpolation of guage-based percipiation and temperature data

In the second course, this study applied Ordinary kriging (OK) and Co-kriging (Co-K) to fill the gaps in meteorological data from Weather stations. These methods been widely used to interpolate temperature point data (Berndt and Haberlandt 2018; Bhunia et al. 2018; Hsu et al. 2017; Tan et al. 2021; Tobin et al. 2011) and precipitation point data (Tan et al. 2021; Zheng et al. 2017; Zou et al. 2021). In this study, data normality was applied to the data of the weather stations in the study area to map precipitation and temperature across the country.

The Kriging technique uses a semivariogram (half of a theoretical variogram) as a measure of variance to detect and depict the spatial correlation between observations. The mathematical functions for calculating semivariograms and describing the degree of spatial dependency are as follows (Cressie 1994; Fanchi 2018; Zimmerman 1994):

$$\gamma(h) = \frac{1}{2N(h)} \sum\nolimits_{i=1}^{N(h)} \left[Z(u_i + h) - Z(u_i) \right]^2 \qquad (10)$$

where $\gamma(h)$ is an empirical semivariogram, N(h) is the number of paired observations with distance h, and $Z(u_i)$ and $Z(u_i + h)$ are the observed values in u_i and $u_i + h$ locations, respectively.

After the empirical half-variance variogram is calculated, the most appropriate model is fitted to the data. The principle of prediction is based on a weighted average of observations in the vicinity of the estimated point values, i.e. $Z(u_i)$. The weight λ_i depends on the distance, and the spatial relationship between observations can be determined through different kriging techniques such as ordinary kriging and universal kriging (Zůvala et al. 2016).

Ordinary kriging as a spatial data interpolator finds the best linear unbiased estimate of a second-order stationary random field with an unknown constant mean as follows (Ali Akbar 2012):

$$\widehat{Z}(u_0) = \sum\nolimits_{i=1}^{n} \lambda i Z(u_i) \qquad (11)$$

where $\widehat{Z}(u_0)$ is the kriging estimate at location u_0, $Z(u_i)$ is the value observed at location u_i, and λ_i is the weighting factor for $Z(u_i)$.

The variance of estimation is:

$$\sigma_{OK}^2(u) = -\gamma(u, u) + \sum\nolimits_{i=1}^{n} \lambda_i \gamma(u, u_i) + \mu \qquad (12)$$

where $\gamma(u, u)$ is the mean of the semivariogram at the estimated location of $u, \gamma(u, u_i)$ is the mean of the semivariogram between location u and the ith location of observation, and μ is the lagrangian coefficient used to minimize the kriging variance. Estimation variance measures the uncertainty of the estimation at a desired point.

The estimation error variance by ordinary kriging is as follows:

$$\widehat{Z}(u_0) - Z(u_0) = R(u_i) = \sum\nolimits_{i=1}^{n} \lambda Z(u_i) - Z(u_0) \qquad (13)$$

where $Z(u_0)$ is an unknown true value at u_0, and $R(u_i)$ is the estimation error. An estimator is unbiased; therefore:

$$E[R(x_0)] = 0 \text{ and } \sum\nolimits_{i=1}^{n} \lambda_i = 1 \qquad (14)$$

The co-kriging technique uses a secondary variable that is spatially interdependent on the main variable. Considering a secondary variable, a classic co-kriging semivariogram is defined as (Cahn et al. 1994):

$$\gamma_{12}(h) = \frac{1}{2N(h)} \sum\nolimits_{i=1}^{N(h)} ([Z_1(x_i + h) - Z_1(x_i)][Z_2(x_i + h) - Z_2(x_i)]) \qquad (15)$$

where $\gamma 12$ is a mutual semivariogram serving as the function of the distance (h), and N is the number of pairs of points $Z_1(x_i)$ and $Z_2(x_i)$ at a stepped distance $(h + dh)$. The co-kriging estimate of the Z_i attribute at position X_0 is calculated by the following equation:

$$Z_i(x_0) = \sum\nolimits_{i=1}^{N(h)} \lambda_{1i} Z_1(x_i) + \sum\nolimits_{i=1}^{N(h)} \lambda_{2i} Z_2(x_i) \qquad (16)$$

where λ_{1i} is the weight associated with $Z_1(x_i)$, and λ_{1i} is the weight of $Z_2(x_i)$.

It should be noted that the purpose of performing the regression method in this study was to estimate gauge observations from satellite measurement whereas, interpolation was performed to fill the data gaps between spatially known ground point data. However, in case spatial data is missing, both methods can also be used for data gap filling, and they are conceptually closely related. In most cases, regression methods are used to identify a generalized function defining the dependent variable from the independent variables at any given point, while interpolation methods used to estimate the values by using the known values at surrounding input points using a function that fairly describes the spatial/temporal distribution of a variable (Madenci et al. 2019).

As the results of the previous two tiers, this study developed four raster maps of air temperature and precipitation were developed for the entire Iran.

2.3.3 Implementation of KG classification scheme

As developed by (Kottek et al. 2006), the KG classification scheme was adopted under the criterion in Tables 2 and 3. Accordingly, five main climate groups are defined each presented with a letter as: (A) tropical climate, (B) arid climate, (C) warm temperate climate, (D) snow climate, and (E) polar climate. Then, each of the climates is divided into smaller climatic zones based on the seasonal variation of precipitation in an area. As a result, there are several classes to define, including dry summer (s), dry winter (w), and no dry season or completely humid climate (f) (Peel et al. 2007). Definitions of these main groups are based on the criterion presented in Table 3.

As shown in Table 3, the first letter describes the climate in term of the temperature condition, and the second letter describes the climate in term of the precipitation conditions in an area. Also, T_{min}, T_{max}, P_{ann}, P_{min}, P_{smin}, P_{smax}, P_{wmin}, and P_{wmax} represent the monthly mean temperature of the coldest month, monthly mean temperature of the hottest month, accumulated annual precipitation, precipitation of the driest month, lowest monthly precipitation values for the summer, highest monthly precipitation values for the summer, lowest monthly precipitation values for the winter, and highest monthly precipitation values for the winter, respectively. The third letter in the KG method is defined based on the criteria shown in Table 3. Note that, for type (b), a threshold temperature value of $+10$ºC is set for at least four months, as defined in the third column of Table 4 (Kottek et al. 2006).

The KG method applies dryness threshold (P_{th}) values for class B climate based on the absolute measure of the annual mean temperature and the annual cycle of precipitation. The following equations show how this threshold is set.

$$P_{th} = 2 \times T_{ann} \quad \text{if at least 2/3 of the annual precipitation occurs in winter} P_{th}$$
$$= 2 \times T_{ann} + 28 \quad \text{if at least 2/3 of the annual precipitation occurs in winter} P_{th}$$
$$= 2 \times T_{ann} + 14 \quad \text{otherwise}$$

(17)

Table 3 The main types of climate in the KG climate classification, descriptions and identification criteria (Kottek et al. 2006)

Type	Description	Criterion
A	Equatorial climates	$T_{min} \geq +18°C$
Af	Equatorial rainforest, fully humid	$P_{min} \geq 60$ mm
Am	Equatorial monsoon	$P_{ann} \geq 25(100-P_{min})$
As	Equatorial savannah with dry summer	$P_{min} < 60$ mm in summer
Aw	Equatorial savannah with dry winter	$P_{min} < 60$ mm in winter
B	Arid climates	$P_{ann} < 10$Pth
Bs	Steppe climate	$P_{ann} > 5$ Pth
Bw	Desert climate	$P_{ann} \leq 5$Pth
C	Warm temperate climates	$-3°C < T_{min} < +18$ °C
Cs	Warm temperate climate with dry summer	$P_{smin} < P_{wmin}, P_{wmax} > 3P_{smin}$ and $P_{smin} < 40$ mm
Cw	Warm temperate climate with dry winter	$P_{wmin} < P_{smin}$ and $P_{smax} > 10$ P_{wmin}
Cf	Warm temperate climate, fully humid	Neither Cs nor Cw
D	Snow climates	$T_{min} \leq -3$ °C
Ds	Snow climate with dry summer	$P_{smin} < P_{wmin}, P_{wmax} > 3P_{smin}$ and $P_{smin} < 40$ mm
Dw	Snow climate with dry winter	$P_{wmin} < P_{smin}$ and $_{Psmax} > 10$ P_{wmin}
Df	Snow climate, fully humid	neither Ds nor Dw
E	Polar climates	$T_{max} < +10$ °C
ET	Tundra climate	0 °C $\leq T_{max} < +10$ °C
EF	Frost climate	$T_{max} < 0°C$

Table 4 Determination of the third letter for the temperature conditions in the KG climate classification method

Type	Description	Criterion
h	Hot steppe /desert	$T_{ann} \geq +18$ °C
k	Cold steppe /desert	$T_{ann} < +18$ °C
a	Hot summer	$T_{max} \geq +22$ °C
b	Warm summer	not (a) and at least 4 $T_{mon} \geq +10$ °C
c	Cool summer and cold winter	not (b) and $T_{min} > -38$ °C
d	extremely continental	like (c) but $T_{min} \leq -38$ °C

T_{ann} is the annual mean near-surface temperature

In total, this study produced six maps in a raster format with spatial resolution of 1000 m. The four maps resulted from MLR models and spatial interpolation per precipitation and temperature. These maps cover the entire country of Iran. This study also produced two further KG classification maps from unused ground-based meteorological data (109 stations) in MLR and spatial interpolation techniques. In line with four other maps, the ground-based KG maps were generated with spatial resolution of 1000 m. However, those only identify the KG classification of each weather observation station. The ground-based maps were used to assess the accuracy of the four other maps against the real meteorological data from weather observation stations.

2.4 Evaluation of model performance

Since the result of practicing the KG method was a nominal classified map, the final results were evaluated with overall accuracy and the Kappa coefficient (K). The arbitrary Kappa of 0.75 was considered excellent. It was calculated with Eq. 18 as follows (Fleiss et al. 2013):

$$K = \frac{[\%agreement\,observed] - [\%agreement\,expected\,by\,chance]}{100\% - [\%agreement\,expected\,by\,chance]} \tag{18}$$

The Kappa coefficient is a measure of the accuracy of maps and is calculated for each matrix using diagonal and marginal elements. It indicates how well the classification agrees with the real data.

3 Results and discussion

3.1 Satellie-based regression analysis

The strength of relationship between meteorological values and satellite-based data was inspected statistically with Pearson's correlation test. Figure 4 shows the relationship between air temperature and three types of MODIS- LST data. The highest correlation was found between T_{min} and LST_{min} followed by the T_{ann}-LST_{ann} and T_{max}-LST_{max} pairs at a ground station. The correlations were significant based on Pearson's correlation test at P-value < 0.01.

As shown in Table 5, there was a significant and positive linear correlation between T_{min} and LST values at the significance level of 0.01. In addition, value of variance inflation factor (VIF) for all the linear models were less than the determined cut-off point value (VIF < 10). This indicates the non-collinearity in the models.

In the case of statistical relationship between ground-based precipitation data and GPM data, correlation generally declined when precipitation decreased. As shown in Fig. 5, the highest correlation belonged to the P_{wmax}-GPM_{wmax} pair, followed by P_{ann}-GPM_{ann}, P_{w}-GPM_{w}, P_{wmin}-GPM_{wmin}, and P_{smin}-GPM_{smin}. This result also indicated overestimation of GPM values among all the developed regression models. Collectively, Pearson's correlations were significant (2-tailed P value < 0.01) for all the pairs (Fig. 5).

Table 6 shows MLR models between ground-based participation (depended variable) and GPM data, TVDI data

Fig. 4 Relationship between T_{ann}-LST_{ann}, T_{max}-LST_{max} and T_{min}-LST_{min} pairs at a ground station
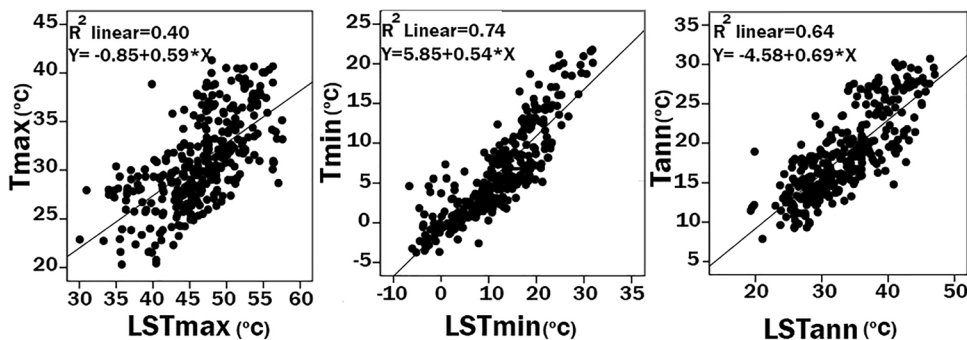

Table 5 Statistics for the regression model output based on the ground-based temperature data

KG input	IV	Equation	R^2	Sig	VIF(s)
T_{min}	DEM, LST_{min}	-0.002*(DEM) + 0.493*(LST_{min}) + 3.250	0.82	0.000	< 5.1
T_{ann}	LST_{ann}, DEM	-0.003*(DEM) + 0.522*(LST_{ann}) + 5.001	0.78	0.000	< 02.1
T_{max}	DEM, LST_{max}	-0.004*(DEM) + 0.449*(LST_{max}) + 14.609	0.65	0.000	< 1.0

LST_{ann} annual mean LST, *LST_{min}* monthly mean LST of the coldest month, *LST_{max}* monthly mean LST of the hottest month, *DEM* digital elevation model

and DEM (independent variables). According to Table 2, with the increase of overall rainfall in a time scale, the correlations between ground data and satellite data are increased. For example, P_{smin} and P_{ann} show the lowest and highest correlation with GPM_{smin} and GPM_{ann} respectively. However, the TVDI as an ancillary independent variable improves the correlations to some extent. Also, VIF values indicated in this table reject collinearities between independent variables.

Figure 6 shows TVDI maps derived from MODIS LST and NDVI products. LST and NDVI on the same time scale were plotted against each other, and LST_{min} and LST_{max} parameters (Table 6) were derived from the triangulated graph presented in Fig. 2. The monthly scatter plots of April, June, August, and October as well as the equations used to calculate LST_{max} and LST_{min} values for mapping TVDI are presented in Fig. 7 and Table 7, respectively. As shown in Fig. 6, most wet areas on all the time scale maps are located in the north and west of the country, but they reduce from the northwest to the southeast. In the eastern and southern regions, the lack of
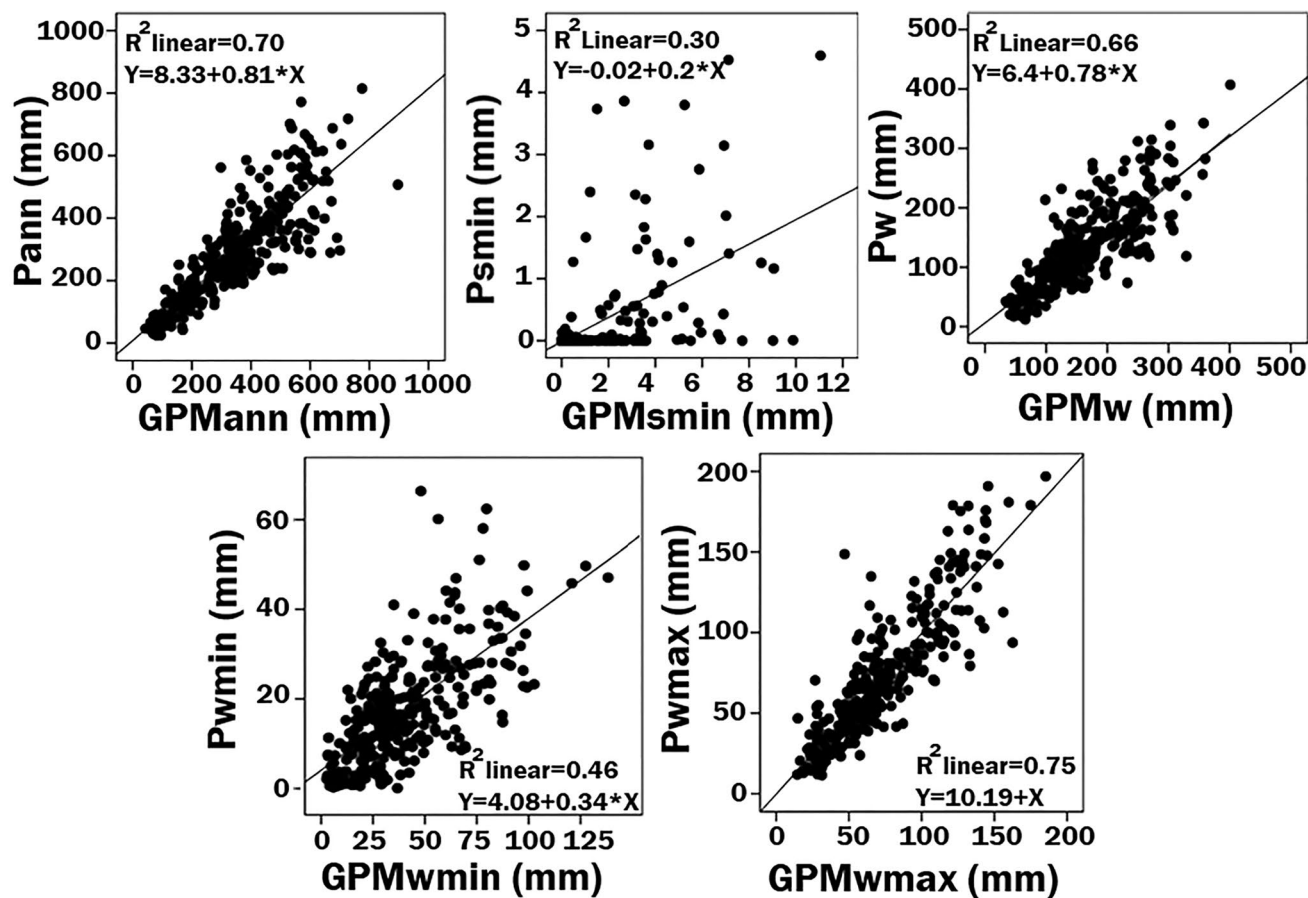

Fig. 5 Relationship between the pairs P_{ann}-GPM_{ann}, P_{smin}–GPM_{smin}, P_{w}-GPM_{w}, P_{wmin}-GPM_{wmin}, and P_{wmax}-GPM_{wmax}

Table 6 Statistics for MLR models output based on the ground-based precipitation data and GPM data, TVDI data and DEM

KG input	IV		Equation	R^2	Sig	VIF(s)
P_{smin}	GPM_{smin}	$TVDI_{smin}$	$2.962*(TVDI_{smin})+0.121*(GPM_{smin})-0.951$	0.27	0.000	< 5.3
P_{wmin}	GPM_{wmin}	$TVDI_{wmin}$	$0.253*(GPM_{wmin})+22.648*(TVDI_{wmin})-4.235$	0.43	0.000	< 4.0
P_{wmax}	GPM_{wmax}	$TVDI_{wmax}$	$2.920*(TVDI_{wmax})+1.009*(GPM_{wmax})-2.81$	0.68	0.000	< 1.5
P_{w}	GPM_{w}	$TVDI_{w}$	$34.63*(TVDI_{w})+0.818(GPM_{w})-16.564$	0.66	0.000	< 3.4
P_{ann}	GPM_{ann}	$TVDI_{ann}$	$114.91*(TVDI_{ann})+0.809(GPM_{ann})-48.38$	0.70	0.000	< 5.1

P_{ann} accumulated annual precipitation, *P_{smin}* the lowest monthly precipitation values for the summer, *P_{wmin}* lowest monthly precipitation values for the winter, *P_{wmax}* highest monthly precipitation values for the winter, and *Pw* mean value of winter precipitation

rainfall and the increase in temperature lead to a decrease in soil moisture. In addition, TVDI accounts for the vegetation conditions influenced by precipitation (Hussain et al. 2023). Briefly, the effect of rainfall is first reflected as the soil moisture, which varies with climate change. Soil moisture, as a storage for precipitation, is one of the key climate variables owing to its significant role in the hydrological cycle (Gruber et al. 2019) as well as energy and biogeochemical cycles. Regarding the role of soil moisture in the climate system, it is known as a basic property for interpreting for monthly to seasonal climate variations and for climate change studies (Jiang et al. 2023). The large-scale alteration in soil moisture availability is a relatively fast response to the climate variation and a significant sign of regional climate change (Allan et al. 2020; Berg and Sheffield 2018). TVDI is a function of soil moisture and vegetation. As vegetation increases, the surface temperature decreases because the leaves absorb the heat for transpiration and cause a reverse process between the surface temperature and the vegetation. However, TVDI reproduces the variation in moisture on a finer scale than can be derived from ground-based data in the study area.

Figure 8 shows modelled precipitation and temperature resulted from regression analysis. As shown, the hottest region of Iran is located mainly in the south and southeast, and the coldest region is in the Northwest part of the country. The mean air temperature is increased from the north to the south and from the west to the east. The increase of temperature in the West–East direction is due to the existence of mountains and the topographic conditions of western Iran. The increase of temperature in the north–south direction is due to the proximity to the equator, the increase in the angle of the sun, and the moisture richness of the atmosphere on the southern coasts.

3.2 Spatial interpolation

Additionally, the ground-based data of rainfall and air temperature were interpolated statistically on different time scales as the required parameters for the KG method. The interpolation was conducted after data normalization, which is a pre-requisite for interpolation (of kriging and Co-kriging types). Considering Root Square Mean Error ((RMSE) values, T_{max}, T_{min}, T_{ann}, P_{swin}, P_{wmax}, P_{ann} and P_{wmin} were interpolated through Co-Krigging method using DEM as an ancillary data. Whereas, ordinary kriging had better performance than Co-kriging method in interpolating P_w point data. Figure 9 shows the maps of geo-statistically
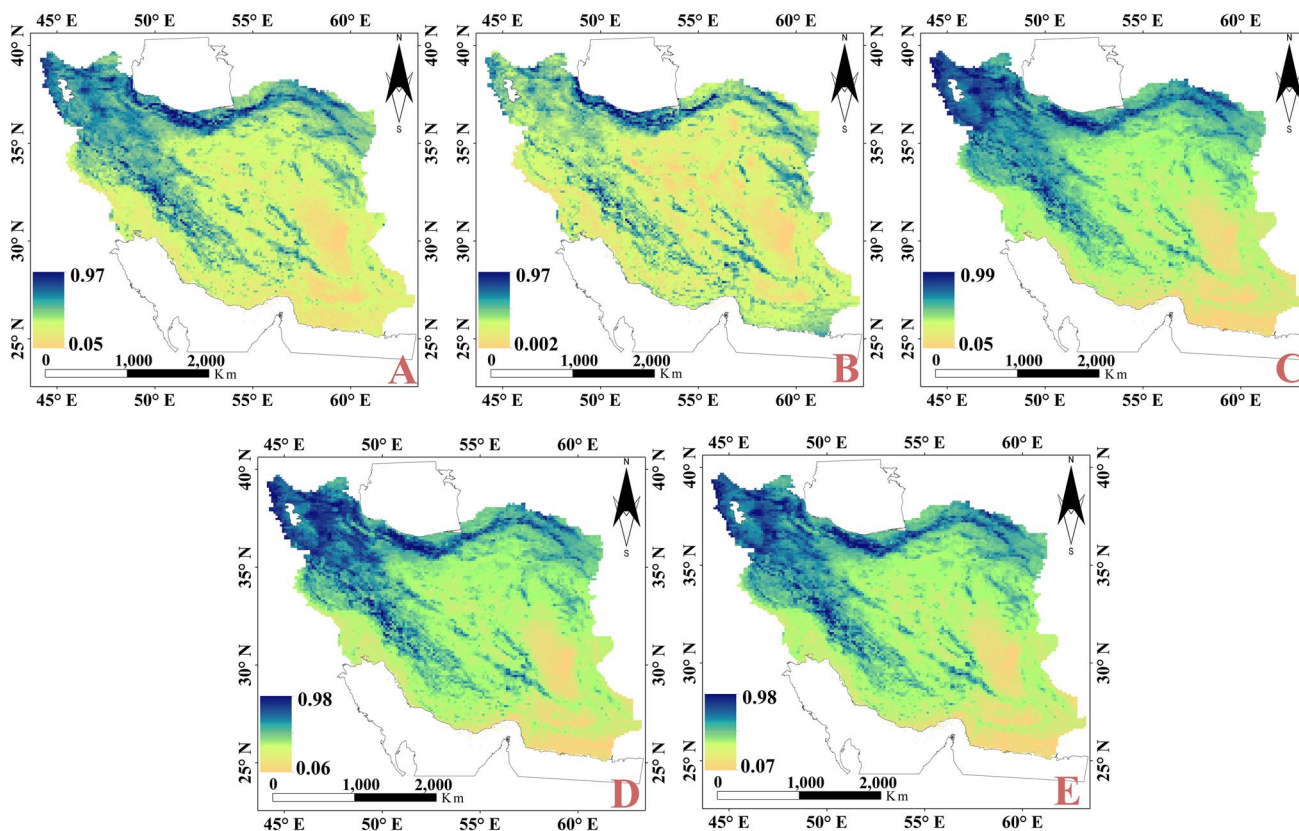

Fig. 6 TVDI maps for different time scales: (**A**) TVDI$_{ann}$, (**B**) TVDI$_{smin}$, (**C**) TVDI$_{wmin}$, (**D**) TVDI$_{wmax}$, and (**E**) TVDI$_{wmin}$
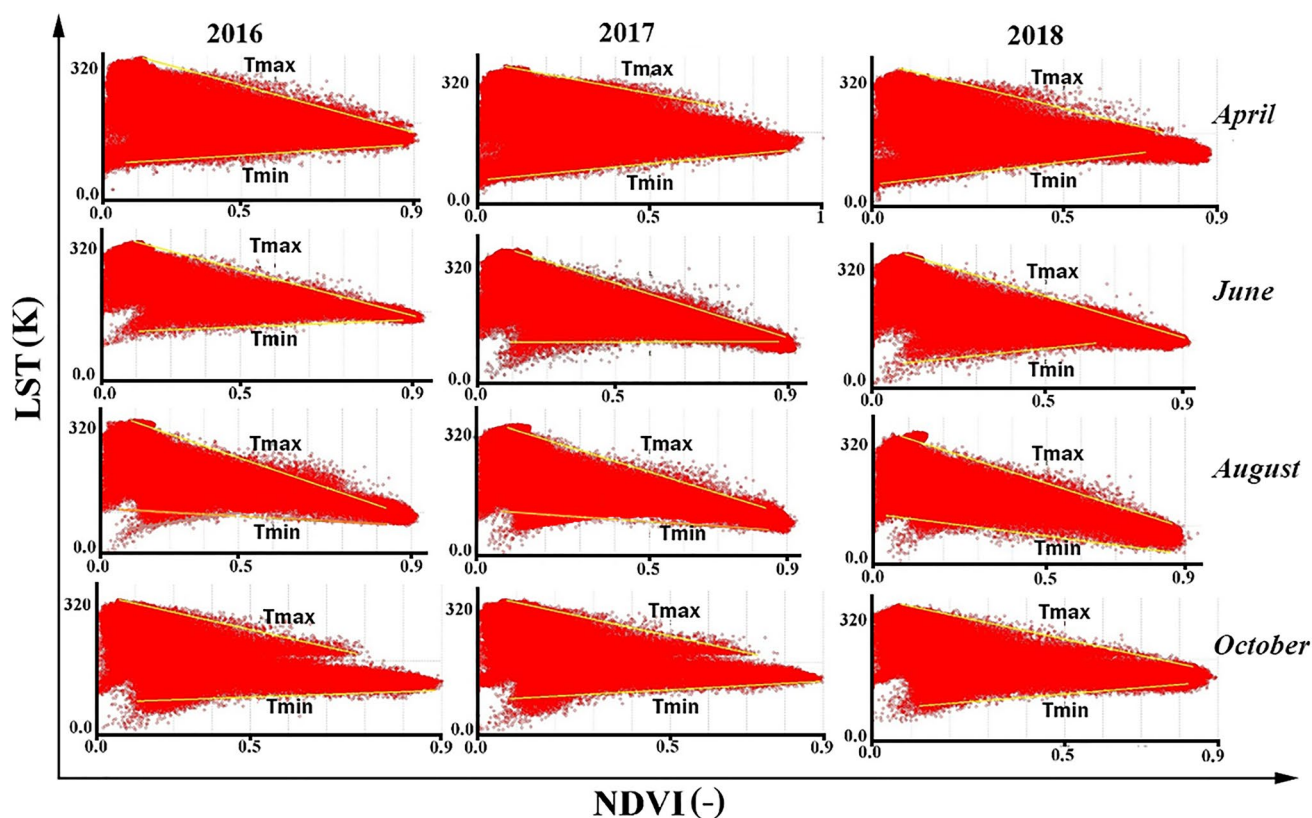
Fig. 7 Scatter plots of LST and NDVI maps on different time scales (for a sample of four months including April, June, August and October)

Table 7 Equation derived from LST-NDVI space in the calculation of LST_{max} and LST_{min} values

Month	Edge	2016	2017	2018
April	Dry	y = -46.316(NDVI) + 340.06	y = -33.19(NDVI) + 337/15	y = -26.984(NDVI) + 334.14
	Wet	y = 12.599(NDVI) + 274.49	y = 18.473(NDVI) + 272/45	y = 23.756(NDVI) + 272.34
June	Dry	y = -50.339(NDVI) + 346.6	y = -39.558(NDVI) + 342/77	y = -44.485(NDVI) + 343.46
	Wet	y = 13.348(NDVI) + 283.03	y = 4.423(NDVI) + 294/05	y = 18.869(NDVI) + 284.99
August	Dry	y = -41.208(NDVI) + 341.96	y = -32.913(NDVI) + 338/44	y = -29.587(NDVI) + 336.28
	Wet	y = 5.725(NDVI) + 294.74	y = 12.882(NDVI) + 294/87	y = -12.091(NDVI) + 299.84
October	Dry	y = -34.044(NDVI) + 327.68	y = -39.118(NDVI) + 331.81	y = -35.632(NDVI) + 330.1
	Wet	y = 6.783(NDVI) + 281.13	y = 14.875(NDVI) + 278/56	y = 12.849(NDVI) + 274.42

Dry Dry edge, *Wet* Wet edge

interpolated ground-based precipitation and air temperature data.

3.3 Demonstration of KG classification maps

Figure 10 shows KG classification maps generated from satellite-based data (KG_s) and ground-based geo-statistically interpolated data (KG_{gs}). Overall, this study identified three main groups and eight sub-groups of KG climate classes in Iran. Based on this classification, the three main types of climates in Iran during 2016–2019 were B (arid climate),

C (warm temperate climate), and D (snow climate). Moreover, the Bwh subgroup (characterized by dry and very hot desert conditions) dominates the largest area of the country, encompassing most of the central parts, southeast, parts of the northeast, and the hillside of the Zagros mountains in the study region. The Bsk subgroup, representing semi-arid and cold desert climates, extends over the east and northeast, as well as parts of the south to southwest, including areas of the Zagros mountains. The Bwk subgroup, associated with dry and cold conditions, covers the northern and western edges of the central part of the country. Following in the hierarchy
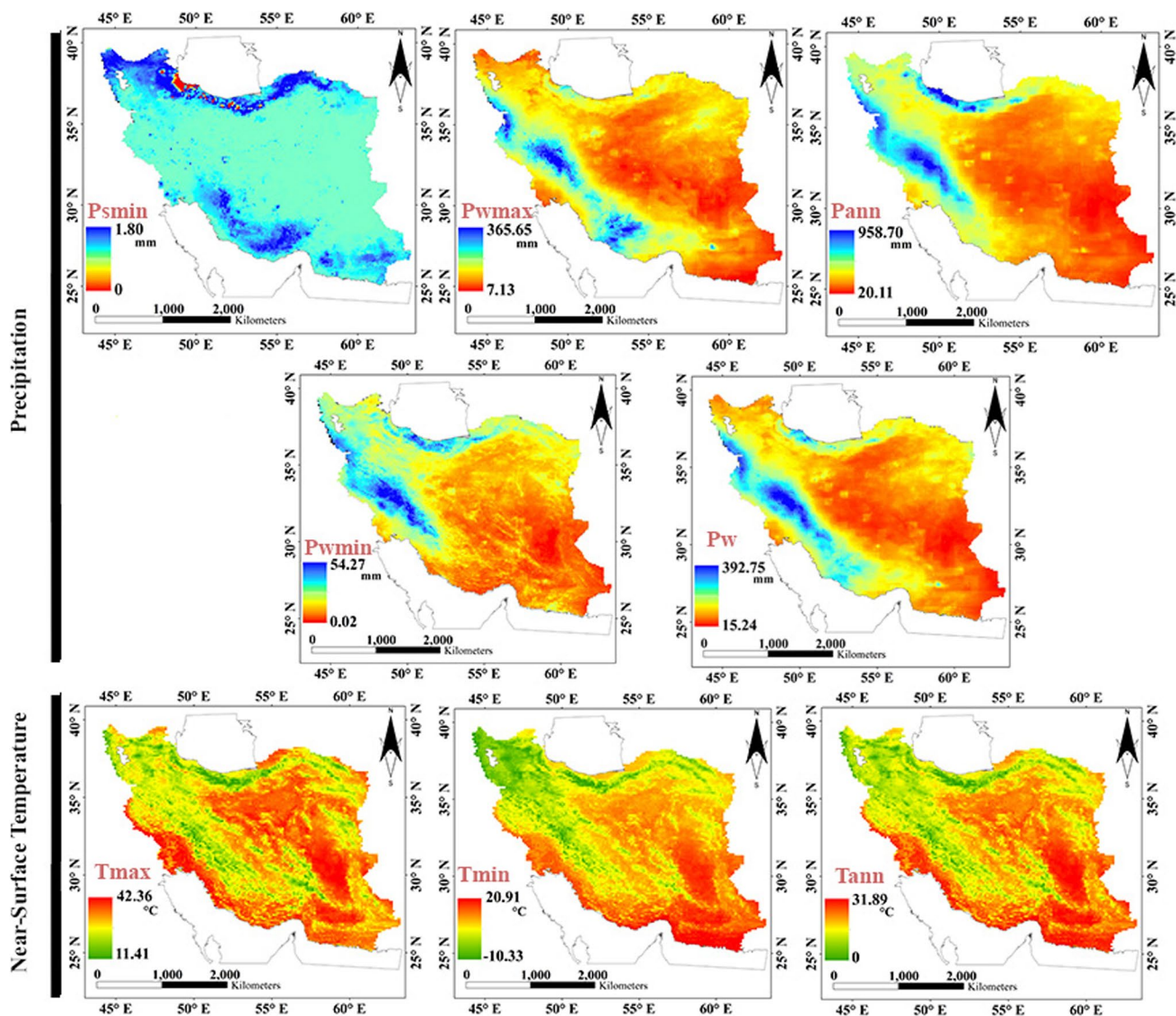
Fig. 8 Regression-based near-surface temperature and precipitation maps

of Group B, the Bsh subgroup, characterized by dry and very hot semi-desert climates, spans from the center to the south and southwest regions. The Csa subgroup, the sole representative of Group C, signifies the Mediterranean climate with dry and very hot summers, spanning from the north to the northwest and southwest of the country. Additionally, the Dsa subgroup, belonging to the cold climate (D), covers the north and northwest regions. Figures 10 and 1 indicate that Dsa, Dsb, and Csb cover only a small portion of the country.

Additionally, Fig. 11 shows a comparison between similarity and differences of the KG main group and sub-group between KG$_{gs}$ and KG$_s$ maps. Overall, the greatest output difference between the two methods belongs to C and D main groups. However, based on the results, the Bwh climate group covers a major part of the country.

Considering KG$_{gs}$ (Figs. 10 and 11), in the main group, similar to KG$_s$, climate B has the largest area covering above 90% of the country, and the predominant sub-climate of the three groups is Bwh, which covers about 55.73% of the country. Bsk, the second dominant climate which covers about 20.47% of the country, has the average annual temperature below 18°C and is extended in the northeastern, northern, and western regions up to the Zagros Mountainous. In terms of area coverage, the third dominant climate of the country is Bwk followed by the sequence of Bsh, Csa, Dsa, Csb and Dsb.

In terms of area coverage, the two methods showed almost similar results. The maximum and minimum area differences between classes of KG$_{gs}$ and KG$_s$ were about 3% (Bwh) and 0.2% (Bsh), respectively. In general, the same
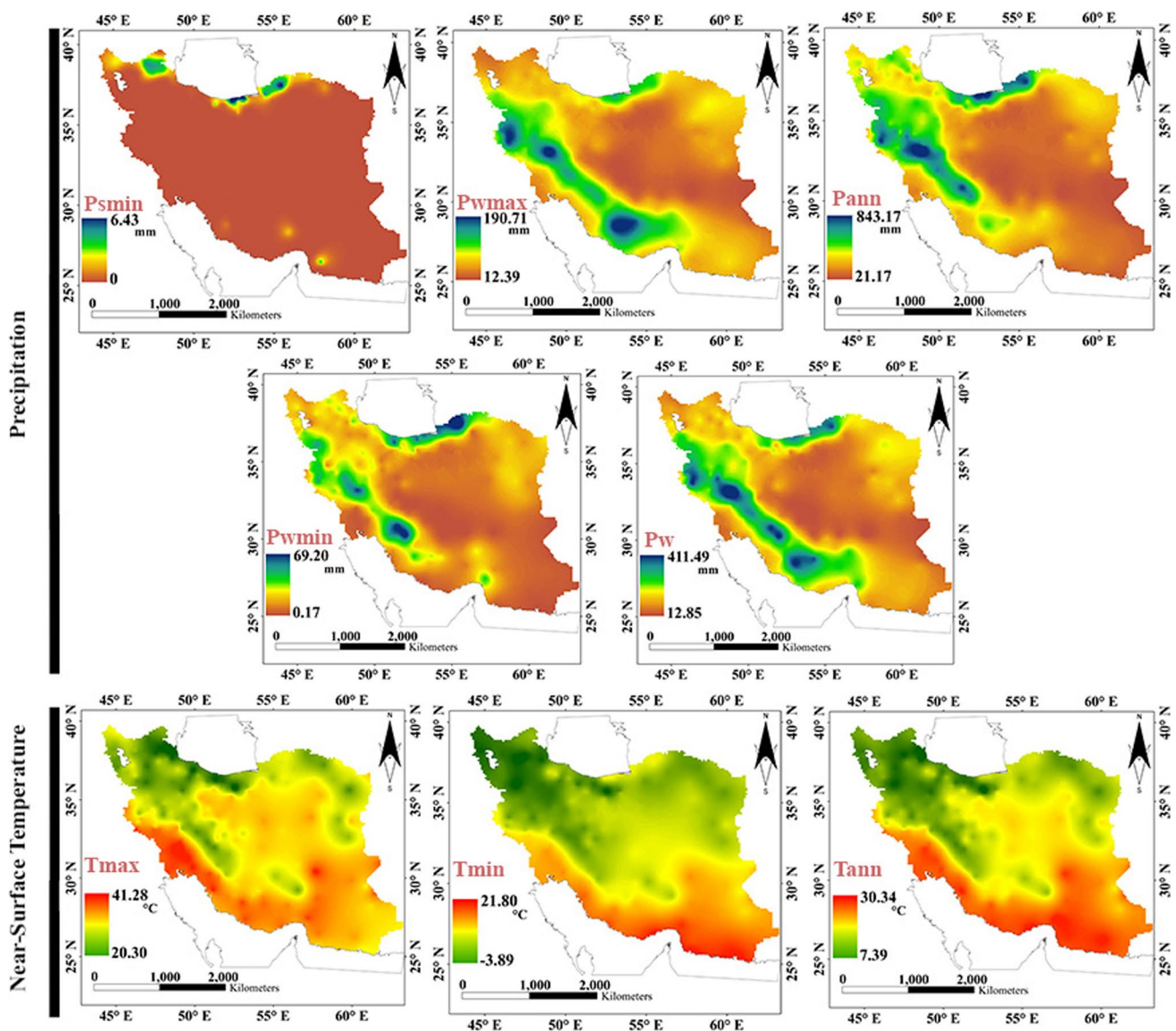
Fig. 9 Geo-statistically interpolated precipitation and air temperature maps based on the ground data of the study area

trend of change can be seen in the areas on both KG$_{gs}$ and KG$_s$ maps.

3.4 Assessment of model performance

As indicated in Table 8, the overall accuracy values of 92.66% and 84.4% and the Kappa coefficients of 0.75% and 0.41% were obtained for KG$_s$ and KG$_{gs}$, respectively. Although the kappa values are obviously different in the main groups, the values obtained by the two methods are closer to each other in the sub-groups. In addition to the kappa, disagreement indices including quantity disagreement (QD) and allocation disagreement (AD) were calculated in this study. The details of equations in calculating

QD and QD have been presented by Pontius and Millones (2011). The inverse behavior of total disagreement (sum of QD and QD values) in contrast to the kappa and total accuracy can be seen in Table 8.

If the point-wise climate classification map (derived from 223 synoptic stations) is overlaid with the GPM and LST images, KG (Tables 9 and 10) can be proposed for the study area

$$P_{th} = 2 \times LST_{ann} \text{ if at least } 3/4 \text{ of the annual precipitation occurs in winter} \tag{19}$$

$$P_{th} = 2 \times LST_{ann} + 38 \text{ otherwise.} \tag{20}$$

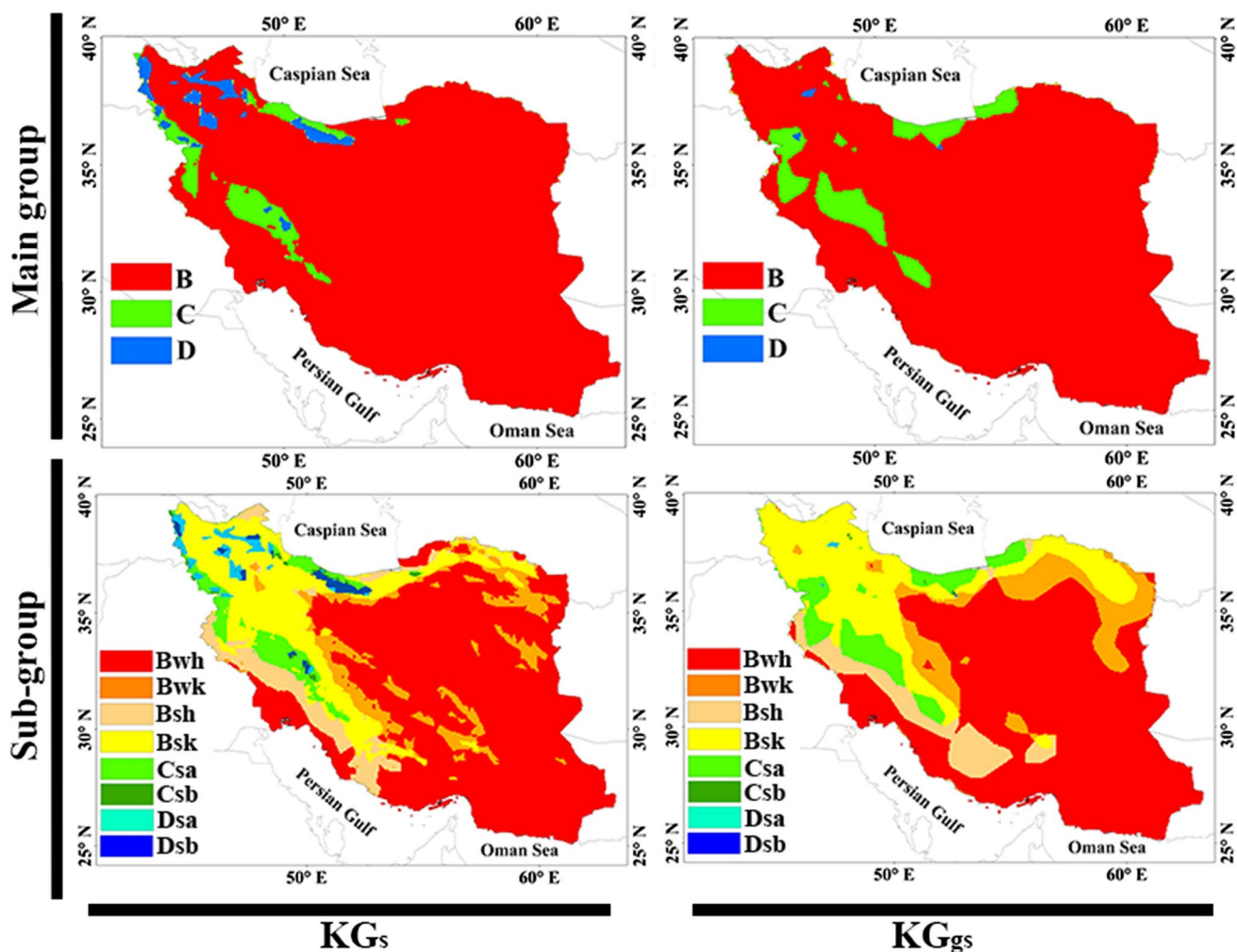The Kappa accuracy was improved where the modified KG criteria were applied on LST and GPM data (Table 11). The

Fig. 10 Main-group and sub-group areas on KG$_s$ and KG$_{gs}$ maps

4 Conclusion

This study provided a comprehensive assessment between regression analysis and spatial interpolation techniques in the use of developing Köppen-Geiger (KG) classification maps on a national scale. Both techniques are popular to overcome data inconsistency and scarcity. In the case of regression analysis, this research examined the relationship between MODIS-LST, MODIS-NDVI, MODIS-TVDI, GPM-precipitation and SRTM-DEM (explanatory variables) and ground-based precipitation and temperature (dependent variables). The spatial interpolation model (Krigging and Co-krigging) was developed from a weather observation station. Overall, this study identified three main groups and eight sub-groups of KG climate classes in Iran. Based on this classification, the three main types of climate in Iran during 2016–2019 were B (arid climate), C (warm temperate climate) and D (snow climate). Also, the results showed that the area coverage of the sub-groups (Bwh, Bsk, Bwk, Bsh, Csa, Dsa, Dsa, Dsb and Csb) in the maps obtained from the two studied methods follow each other to a large extent.

This research study thus obtained a Kappa of 66% for the sub-group on the KG$_{gs}$ map. The results also revealed that the KG map generated from satellite data was more accurate than the map generated from geostatistically

Fig. 11 Comparison of the percentages for different main-group and sub-group areas on KG$_s$ and KG$_{gs}$ maps
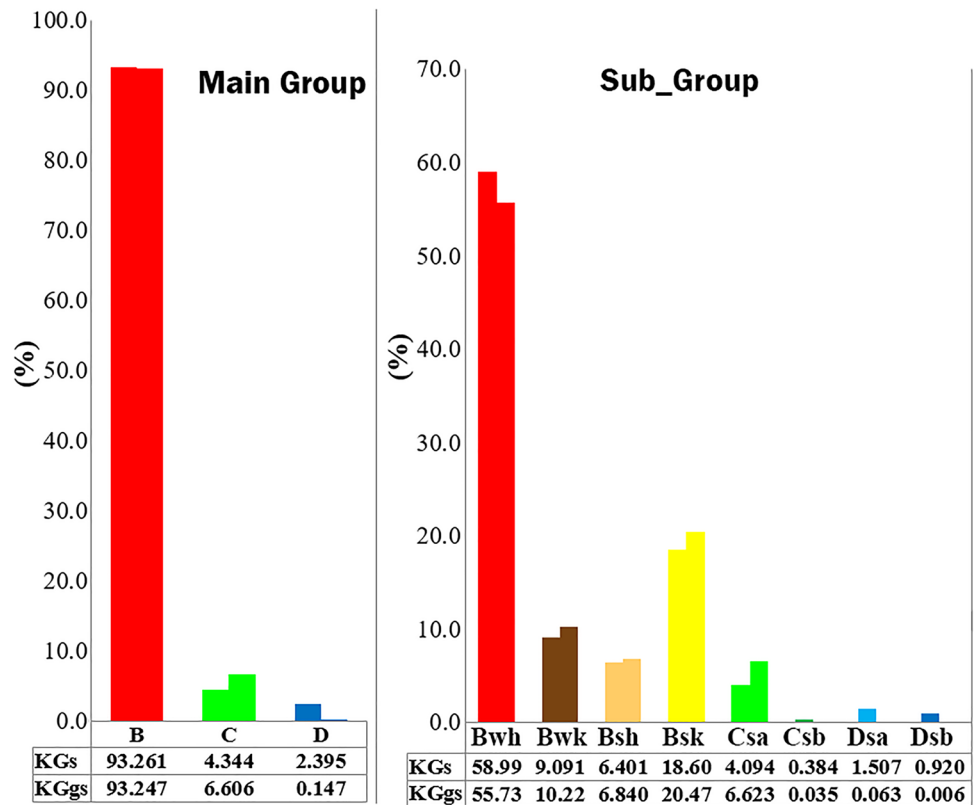

	B	C	D
KGs	93.261	4.344	2.395
KGgs	93.247	6.606	0.147

	Bwh	Bwk	Bsh	Bsk	Csa	Csb	Dsa	Dsb
KGs	58.99	9.091	6.401	18.60	4.094	0.384	1.507	0.920
KGgs	55.73	10.22	6.840	20.47	6.623	0.035	0.063	0.006

Table 8 Kappa statistics, the overall accuracy, QD and AD of KG$_s$ and KG$_{gs}$ maps based on the test data

Classifications	Overall Accuracy (%)		Kappa (%)		Quantity disagreement (%)		Allocation disagreemet		Total disagreement (%)	
	KG$_s$	KG$_{gs}$	KG$_s$	KG$_{gs}$	KG$_s$	KG$_{gs}$	KG$_s$	KG$_{gs}$	KG$_s$	KG$_{gs}$
The main grouping	92.66	84.40	75	41	7	10	0	6	7	16
Subgroup (subgroups)	77.98	73.64	71	66	12	13	11	13	23	26

Table 9 Determination of the KG main group and criteria in case of using LST and GPM satellite data

Type	Description	Criterion
B	Arid climates	$GPM_{ann} < 6Pth$
Bs	Steppe climate	$GPM_{ann} > 3pth$
Bw	Desert climate	$GPM_{ann} \leq 3pth$
C	Warm temperate climates	$-5\ °C < LST_{min} < 30\ °C$
Cs	Warm temperate climate with dry summer	$GPM_{smin} < GPM_{wmin}$, $GPM_{wmax} > 3*$ GPM_{smin}, $GPM_{smin} < 40$ mm
D	Snow climates	$LST_{min} \leq -5\ °C$
Ds	Snow climate with dry summer	$GPM_{smin} < GPM_{wmin}$, $GPM_{wmax} > 3*$ GPM_{smin}, $GPM_{smin} < 40$ mm

Table 10 Determination of the third letter (temperature conditions) in the KG climate classification method with LST data

Type	Description	Criterion
h	Hot steppe / desert	$LST_{ann} \geq 32\ °C$
k	Cold steppe /desert	$LST_{ann} < 32\ °C$
a	Hot summer	$LST_{max} \geq 30\ °C$

Table 11 Kappa statistics for the overall accuracy of climate classification based on the modified KG criteria

Classifications	Overall Accuracy(%)	Kappa(%)
The main grouping	99.38	0.88
Subgroup (subgroups)	93.37	0.86

interpolated ground data. Due to the operational applicability of remotely sensed data, this study claims to be of insight for climate classification based on remote sensing imageries. The spatial trends of climate change can also be detected with continuous pixel-based data. However, with the Kappa of at least 75%, this study showed that satellite data can be used for KG climate classification, although GPM data and point data are not homologous. The dissimilarity of satellite data and point data may be due to the high spatial variation of precipitation in arid and semi-arid regions, whereas satellite data estimate precipitation with 10-km spatial resolution. Satellite data helps to define a new threshold, modify the criteria, and offer a new approach to examining climate globally.

Continuous pixel-based climate maps created from the presented methodology are expected to reveal better climate transition zones than the point data. Moreover, overlying time series climate maps generated from long-term satellite data the maps of future climate zones can be generated and the hotspots of environmentally susceptible areas due to climate change and climate warming can be identified. Due to the global coverage of satellite data, a unique and globally high temporal and spatial resolution climate map can be generated, and significant regional and temporal climate change can be portrayed. However, this study recommends employing techniques such as artificial intelligence for data gap filling of climate data with the purpose of climate classification. This study also suggests the evaluation of the performance of the presented methodology in the area covering KG climate classes other than classes existing in the study area of this research.

Declarations

Competing interests The authors declare no competing interests.

References

Aboutalebi M, Torres-Rua AF, Allen N (2018) Spatial and Temporal Analysis of Precipitation and Effective Rainfall Using Gauge Observations Satellite, and Gridded Climate Data for Agricultural Water Management in the Upper. Colo River Basin Remote Sens 10:2058

Akhavan S, Mousabeygi F, Peel MC (2018) Assessment of eight reference evapotranspiration (ETo) methods considering Köppen climate class in Iran. Hydrol Sci J 63:1468–1481. https://doi.org/10.1080/02626667.2018.1513654

Aksu H, Yaldiz SG, Taflan GY, Akgül MA (2023) Frequency analysis based on Peaks-Over-Threshold approach for GPM IMERG precipitation product. Theoret Appl Climatol 154:275–289. https://doi.org/10.1007/s00704-023-04555-5

Ali Akbar D (2012) Reserve estimation of central part of Choghart north anomaly iron ore deposit through ordinary kriging method International Journal of. Min Sci Technol 22:573–577. https://doi.org/10.1016/j.ijmst.2012.01.022

Allan RP et al (2020) Advances in understanding large-scale responses of the water cycle to climate change. Ann N Y Acad Sci 1472:49–75. https://doi.org/10.1111/nyas.14337

Amiri MJ, Eslamian SS (2010) Investigation of climate change in Iran. Environ Sci Technol 3:208–216

Ascencio-Vásquez J, Brecl K, Topič M (2019) Methodology of Köppen-Geiger-Photovoltaic climate classification and implications to worldwide mapping of PV system performance. Sol Energy 191:672–685. https://doi.org/10.1016/j.solener.2019.08.072

Atkinson PM, Lloyd CD (2014) Geostatistical Models and Spatial Interpolation. In: Fischer MM, Nijkamp P (eds) Handbook of Regional Science. Springer Berlin Heidelberg, Berlin, Heidelberg, pp 1461–1476. https://doi.org/10.1007/978-3-642-23430-9_75

Beck HE, Zimmermann NE, McVicar TR, Vergopolan N, Berg A, Wood EF (2018) Present and future Köppen-Geiger climate classification maps at 1-km resolution. Sci Data 5:180214. https://doi.org/10.1038/sdata.2018.214

Berg A, Sheffield J (2018) Soil Moisture-Evapotranspiration Coupling in CMIP5 Models: Relationship with Simulated Climate and Projections. J Clim 31:4865–4878. https://doi.org/10.1175/JCLI-D-17-0757.1

Berndt C, Haberlandt U (2018) Spatial interpolation of climate variables in Northern Germany—Influence of temporal resolution and network density. J Hydrol: Reg Stud 15:184–202. https://doi.org/10.1016/j.ejrh.2018.02.002

Bhunia GS, Shit PK, Maiti R (2018) Comparison of GIS-based interpolation methods for spatial distribution of soil organic carbon (SOC). J Saudi Soc Agric Sci 17:114–126. https://doi.org/10.1016/j.jssas.2016.02.001

Bonsoms J, Ninyerola M (2024) Comparison of linear, generalized additive models and machine learning algorithms for spatial climate interpolation. Theor Appl Climatol 155:1777–1792. https://doi.org/10.1007/s00704-023-04725-5

Cahn MD, Hummel JW, Brouer BH (1994) Spatial Analysis of Soil Fertility for Site-Specific Crop Management. Soil Sci Soc Am J 58:1240–1248. https://doi.org/10.2136/sssaj1994.03615995005800040035x

Canan F, Golasi I, Falasca S, Salata F (2020) Outdoor thermal perception and comfort conditions in the Köppen-Geiger climate category BSk One-Year Field Survey and Measurement Campaign in Konya, Turkey. Sci Total Environ 738:140295. https://doi.org/10.1016/j.scitotenv.2020.140295

Cressie N (1994) 4 - Models For Spatial Processes. In: Stanford JL, Vardeman SB (eds) Methods in Experimental Physics, vol 28. Academic Press, pp 93–124. https://doi.org/10.1016/S0076-695X(08)60254-9

Cui D, Liang S, Wang D, Liu Z (2021) A 1 km global dataset of historical (1979–2013) and future (2020–2100) Köppen-Geiger climate classification and bioclimatic variables. Earth Syst Sci Data 13:5087–5114. https://doi.org/10.5194/essd-13-5087-2021

de Moraes RBF, Gonçalves FV (2023) Comparison of the performance of estimated precipitation data via remote sensing in the Midwest Region of Brazil. Theoret Appl Climatol 153:1105–1116. https://doi.org/10.1007/s00704-023-04523-z

Deyasi A, Bhattacharjee AK, Mukherjee S, Sarkar A (2021) Multilayer Perceptron based Comparative Analysis between CNTFET

and Quantum Wire FET for Optimum Design Performance Solid State. Electron Lett 3:42–52. https://doi.org/10.1016/j.ssel.2021.12.003

Every JP, Li L, Dorrell DG (2020) Köppen-Geiger climate classification adjustment of the BRL diffuse irradiation model for Australian locations. Renewable Energy 147:2453–2469. https://doi.org/10.1016/j.renene.2019.09.114

Fallah B, Sodoudi S, Russo E, Kirchner I, Cubasch U (2017) Towards modeling the regional rainfall changes over Iran due to the climate forcing of the past 6000 years. Quat Int 429:119–128. https://doi.org/10.1016/j.quaint.2015.09.061

Fallmann J, Emeis S (2020) How to bring urban and global climate studies together with urban planning and architecture? Dev Built Environ 4:100023. https://doi.org/10.1016/j.dibe.2020.100023

Fanchi JR (2018) Chapter 2 - Geological Modeling. In: Fanchi JR (ed) Principles of Applied Reservoir Simulation (Fourth Edition). Gulf Professional Publishing, pp 9–33. https://doi.org/10.1016/B978-0-12-815563-9.00002-1

Fleiss JL, Levin B, Paik MC (2013) Statistical Methods for Rates and Proportions. Wiley

Francisco E (2014) A New Methodology for Building Local Climate Change Scenarios: A Case Study of Monthly Temperature Projections for Mexico City. Atmósfera 27:429–449. https://doi.org/10.1016/S0187-6236(14)70040-2

Geiger R (1961) Überarbeitete Neuausgabe von Geiger, R.: Köppen-Geiger Überarbeitete Neuausgabe von Geiger, R.: Köppen-Geiger / Klima der Erde. (Wandkarte 1:16 Mill.) – Klett-Perthes, Gotha

Ghajarnia N et al (2022) Evaluating the Evolution of ECMWF Precipitation Products Using Observational Data for Iran: From ERA40 to ERA5. Earth Space Sci 9:e2022EA002352. https://doi.org/10.1029/2022EA002352

Gruber A, Scanlon T, van der Schalie R, Wagner W, Dorigo W (2019) Evolution of the ESA CCI Soil Moisture Climate Data Records and Their Underlying Merging Methodology. Earth Syst Sci Data 11:717–739. https://doi.org/10.5194/essd-11-717-2019

Hammann AC, MacDonell S (2022) Regression-based gap-filling methods show air temperature reductions and wind pattern changes during the 2019 total eclipse in Chile. Sci Rep 12:7718. https://doi.org/10.1038/s41598-022-10623-z

Hobbi S, Michael Papalexiou S, Rupa Rajulapati C, Nerantzaki SD, Markonis Y, Tang G, Clark MP (2022) Detailed investigation of discrepancies in Köppen-Geiger climate classification using seven global gridded products. J Hydrol 612:128121. https://doi.org/10.1016/j.jhydrol.2022.128121

Hooker J, Duveiller G, Cescatti A (2018) A Global Dataset of Air Temperature Derived from Satellite Remote Sensing and Weather Stations. Sci Data 5:180246. https://doi.org/10.1038/sdata.2018.246

Hsu S, Mavrogianni A, Hamilton I (2017) Comparing Spatial Interpolation Techniques of Local Urban Temperature for Heat-related Health Risk Estimation in a Subtropical City. Procedia Engineering 198:354–365. https://doi.org/10.1016/j.proeng.2017.07.091

Hussain A et al (2023) Corrigendum to "Assessment of precipitation extremes and their association with NDVI, monsoon and oceanic indices over Pakistan." Atmos Res 294:106973. https://doi.org/10.1016/j.atmosres.2023.106973

Javanshiri Z, Pakdaman M, Falamarzi Y (2021) Homogenization and trend detection of temperature in Iran for the period 1960–2018. Meteorol Atmos Phys 133:1233–1250. https://doi.org/10.1007/s00703-021-00805-1

Jiang K et al (2023) Combined Influence of Soil Moisture and Atmospheric Humidity on Land Surface Temperature under Different Climatic Background. iScience 26:106837. https://doi.org/10.1016/j.isci.2023.106837

Kebriya Y, Nadi M, Jamei M (2021) Combining interpolation methods and precipitation products of TRMM satellite to increase the accuracy of rainfall maps in Mazandaran province. J Water Soil Conserv 28:49–70. https://doi.org/10.22069/jwsc.2022.19286.3477

Köppen W (1936) Das geographische System der Klimate. Handbuch der Klimatologie vol 1. C. Verlag von Gebrüder Borntraeger, Berlin.

Kottek M, Grieser J, Beck C, Rudolf B, Rubel F (2006) World map of the Köppen-Geiger climate classification updated. Meteorol Z 15:259–263. https://doi.org/10.1127/0941-2948/2006/0130

Ma Q, Li Y, Feng H, Yu Q, Zou Y, Liu F, Pulatov B (2021) Performance evaluation and correction of precipitation data using the 20-year IMERG and TMPA precipitation products in diverse subregions of China. Atmos Res 249:105304. https://doi.org/10.1016/j.atmosres.2020.105304

Madenci E, Barut A, Dorduncu M (2019) Interpolation, Regression, and Smoothing. In: Madenci E, Barut A, Dorduncu M (eds) Peridynamic Differential Operator for Numerical Analysis. Springer International Publishing, Cham, pp 57–90. https://doi.org/10.1007/978-3-030-02647-9_4

Mazzeo D, Baglivo C, Matera N, De Luca P, Congedo PM, Oliveti G (2020) Energy and Economic Dataset of the Worldwide Optimal Photovoltaic-Wind Hybrid Renewable Energy Systems. Data Brief 33:106476. https://doi.org/10.1016/j.dib.2020.106476

McGibbon M, Money-Kyrle S, Blay V, Houston DR (2023) SCORCH: Improving structure-based virtual screening with machine learning classifiers, data augmentation, and uncertainty estimation. J Adv Res 46:135–147. https://doi.org/10.1016/j.jare.2022.07.001

Mokhtari MH, Adnan R, Busu I (2013) A new approach for developing comprehensive agricultural drought index using satellite-derived biophysical parameters and factor analysis method. Nat Hazards 65:1249–1274. https://doi.org/10.1007/s11069-012-0408-x

Moosavi V, Talebi A, Mokhtari MH, Hadian MR (2016) Estimation of spatially enhanced soil moisture combining remote sensing and artificial intelligence approaches. Int J Remote Sens 37:5605–5631. https://doi.org/10.1080/01431161.2016.1244366

Ouatiki H, Boudhar A, Chehbouni A (2023) Accuracy assessment and bias correction of remote sensing–based rainfall products over semiarid watersheds. Theor Appl Climatol 154:763–780. https://doi.org/10.1007/s00704-023-04586-y

Ouma Y, Tjitemisa T, Segobye M, Moreri K, Nkwae B, Maphale L, Manisa B (2021) Urban land surface temperature variations with LULC, NDVI and NDBI in semi-arid urban environments: case study of Gaborone City, Botswana (1989–2019), vol 11864. SPIE, SPIE Remote Sensing

Peel MC, Finlayson BL, McMahon TA (2007) Updated world map of the Köppen-Geiger climate classification Hydrol Earth. Syst Sci 11:1633–1644. https://doi.org/10.5194/hess-11-1633-2007

Pontius RG Jr, Millones M (2011) Death to Kappa: birth of quantity disagreement and allocation disagreement for accuracy assessment. Int J Remote Sens 32:4407–4429. https://doi.org/10.1080/01431161.2011.552923

Pražnikar J (2017) Particulate matter time-series and Köppen-Geiger climate classes in North America and Europe. Atmos Environ 150:136–145. https://doi.org/10.1016/j.atmosenv.2016.11.056

Razmi R, Balyani S, Mansouri Daneshvar MR (2017) Geo-statistical modeling of mean annual rainfall over the Iran using ECMWF database Spatial. Inf Res 25:219–227. https://doi.org/10.1007/s41324-017-0097-3

Salata F, Golasi I, Treiani N, Plos R, de Lieto VA (2018) On the outdoor thermal perception and comfort of a Mediterranean subject across other Koppen-Geiger's climate zones. Environ Res 167:115–128. https://doi.org/10.1016/j.envres.2018.07.011

Sandholt I, Rasmussen K, Andersen J (2002) A simple interpretation of the surface temperature/vegetation index space for assessment of surface moisture status. Remote Sens Environ 79:213–224. https://doi.org/10.1016/S0034-4257(01)00274-7

Sohoulande CDD (2024) Vegetation and water resource variability within the Köppen-Geiger global climate classification scheme: a probabilistic interpretation. Theoret Appl Climatol 155:1081–1092. https://doi.org/10.1007/s00704-023-04682-z

Tabachnick BG, Fidell LS (eds) (2007) Using Multivariate Statistics. F I F T, H. Pearson Education, Boston

Tan J, Xie X, Zuo J, Xing X, Liu B, Xia Q, Zhang Y (2021) Coupling random forest and inverse distance weighting to generate climate surfaces of precipitation and temperature with Multiple-Covariates. J Hydrol 598:126270. https://doi.org/10.1016/j.jhydrol.2021.126270

Tobin C, Nicotina L, Parlange MB, Berne A, Rinaldo A (2011) Improved interpolation of meteorological forcings for hydrologic applications in a Swiss Alpine region. J Hydrol 401:77–89. https://doi.org/10.1016/j.jhydrol.2011.02.010

Wigmore O, Mark B, McKenzie J, Baraer M, Lautz L (2019) Sub-metre mapping of surface soil moisture in proglacial valleys of the tropical Andes using a multispectral unmanned aerial vehicle. Remote Sens Environ 222:104–118. https://doi.org/10.1016/j.rse.2018.12.024

Yoo J, Rohli RV (2016) Global distribution of Köppen-Geiger climate types during the Last Glacial Maximum Mid-Holocene, and Present Palaeogeography, Palaeoclimatology. Palaeoecology 446:326–337. https://doi.org/10.1016/j.palaeo.2015.12.010

Zheng Y, He Y, Chen X (2017) Spatiotemporal pattern of precipitation concentration and its possible causes in the Pearl River basin China. J Clean Prod 161:1020–1031. https://doi.org/10.1016/j.jclepro.2017.06.156

Zimmerman DL (1994) 13 - Statistical Analysis of Spatial Data. In: Stanford JL, Vardeman SB (eds) Methods in Experimental Physics, vol 28. Academic Press, San Diego, pp 375–402. https://doi.org/10.1016/S0076-695X(08)60263-X

Zou W-y, Yin S-q, Wang W-t (2021) Spatial interpolation of the extreme hourly precipitation at different return levels in the Haihe River basin. J Hydrol 598:126273. https://doi.org/10.1016/j.jhydrol.2021.126273

Zůvala R, Fišerová E, Marek L (2016) Mathematical aspects of the kriging applied on landslide in Halenkovice (Czech Republic). Open Geosci 8:275–288. https://doi.org/10.1515/geo-2016-0023